European Conference on Computational Fluid Dynamics
ECCOMAS CFD 2006
P. Wesseling, E. Oñate and J. Périaux (Eds)
© TU Delft, The Netherlands, 2006

REAL-GAS EFFECTS IN ORC TURBINE FLOW SIMULATIONS: INFLUENCE OF THERMODYNAMIC MODELS ON FLOW FIELDS AND PERFORMANCE PARAMETERS

P. Colonna*, **S. Rebay**†, **J. Harinck*** **and A. Guardone**††

*Process and Energy Department, Delft University of Technology
Mekelweg, 2, 2828 CD Delft, The Netherlands, e-mail: P.Colonna@3mE.TUdelft.nl
†Dipartimento di Ingegneria Meccanica, Università di Brescia
Via Branze, 38, 25123 Brescia, Italy
††Dipartimento di Ingegneria Aerospaziale, Politecnico di Milano
Via La Masa, 34, 20159 Milano, Italy

Key words: Turbomachinery, organic Rankine cycle, siloxane, dense gas, real gas, Euler solver, equations of state

Abstract. *The analysis and design of turbomachinery is usually performed by means of fluid dynamic computations employing ideal gas laws. This can lead to inaccurate predictions for Organic Rankine Cycle (ORC) turbines, which operate partly in the non-ideal thermodynamic region. The objective of this work is to evaluate the influence of different equations of state (EoS) on the computed aerodynamic performance and the test case is a 2D nozzle blade of an existing ORC turbine operated with the siloxane MDM as working fluid. Three different fluid models are considered, the simple polytropic ideal gas law, the Peng-Robinson-Stryjek-Vera cubic EoS and the state-of-the-art Span-Wagner EoS. A comparison of the computed Mach number and pressure coefficient distribution along the blade as well as the outlet flow angles, mass flows and loss estimations for both design and off-design operating conditions is presented. The fluid dynamic results are very similar for the computations employing the Span-Wagner and Peng-Robinson-Stryjek-Vera EoS. The calculations performed with the polytropic ideal gas EoS, on the other hand, show large relative differences in almost all parameters, if compared to the accurate Span-Wagner EoS.*

1 INTRODUCTION

In most cases, performance assessments and designs of turbomachinery are based on computational fluid dynamics (CFD) simulations employing the ideal gas law to describe the fluid thermodynamic properties. This choice is based on the assumption that the deviation of the real thermodynamic behavior from ideality is small, which should result in equally small deviations in the predicted flow field and calculated performance parameters. This assumption can be misleading when predicting performance parameters and flow features of turbomachinery that operates, at least partly, in a thermodynamic region where the ideal gas assumption does not hold. This is particularly relevant for Organic Rankine Cycle (ORC) turbines.

Several recent studies on the computation of real-gas flows over airfoils or cascade configurations are reported in the literature. As an example, turbulent viscous real gas flows are computed in[1] using an heterogeneous thermodynamic model to simulate the flow through the nozzle of a radial ORC turbine. The simulation of a steam turbine stage is presented in[2] and employs a look-up table approach to compute the fluid properties from the IAPWS standard thermodynamic model for water. A three-dimensional viscous CFD solver for turbomachinery applications using a local fitting to property tables for the calculation of the fluid properties is presented in[3]. A similar solver employing a modified Redlich-Kwong equation of state (EoS) is shown in[4].

The objective of this work is to evaluate the influence of different equations of state (EoS) on the computed aerodynamic performance of an ORC turbine blade. The flow field through the 2D nozzle blade of an existing turbine operated with the siloxane MDM as working fluid is chosen as an example. The fluid is modeled with the polytropic (i.e., with constant specific heats) ideal gas law, the Peng-Robinson-Stryjek-Vera cubic EoS and the state-of-the-art Span-Wagner EoS. The thermodynamic models considered are of increasing complexity and accuracy and therefore require increasing computational resources.

The evaluation of the different thermodynamic models has been performed by means of inviscid flow simulations which, in the case of attached flows at high Reynolds number, allows an accurate computation of aerodynamic loads, outlet flow angles and mass flows. All the above mentioned quantities are expected to be affected by the thermodynamic description of the fluid.

The CFD computations have been performed with the novel *zFlow* program.[5] The distinguishing features of this code are (1) the usage of a high resolution upwind space discretization method for general unstructured and hybrid grids which are very well suited for the accurate computation of high Mach number flows and allows for high geometrical flexibility and versatility, (2) the use of an implicit time integration scheme which proved to be crucial for the effective computations of fluids characterized by complex and therefore very computationally demanding EoS, and (3) the integration with an extensive library of thermodynamic models for both pure fluids and mixtures which allows for the realistic simulation of fluid flow phenomena which cannot be predicted by means of the simple polytropic ideal gas model commonly employed by most CFD codes.

The effect of the different fluid models on the flow field through the nozzle blade is evaluated by comparing Mach number fields, pressure coefficient and Mach number distributions along the blade, outlet flow angles, mass flows and shock losses for both design and off-design operating conditions. It is however to be noticed that this nozzle has been designed for inlet conditions corresponding to a slightly superheated vapor at a reduced pressure $P/P_\mathrm{c} \approx 0.6$. Significant real gas effects are therefore present only in the initial phase of the expansion through the nozzle blade. Therefore the predicted performance of the nozzle blade is not expected to be heavily affected by the chosen thermodynamic model.

Conclusions are drawn on the difference (magnitude and trends) in ORC turbine performance caused by the (in)accuracy of the adopted EoS model. The sensitivity of the turbine performance to the accuracy of the EoS model and the operating condition has important consequences for the design of ORC turbines.

2 THE EULER SOLVER AND THE ADVANCED THERMODYNAMIC MODELS

2.1 The Euler solver

The numerical solution of the 2D inviscid Navier-Stokes (Euler) equations has been performed with the novel *zFlow* program.[5] The main features characterizing the CFD code *zFlow* are briefly summarized. The spatial approximation of the inviscid Navier-Stokes (Euler) equations is constructed with an high resolution finite volume method suitable for general unstructured and hybrid grids. The method can be regarded as an hybrid between the Finite Element (FE) and Finite Volume (FV) methods in that the finite volume metric quantities are formulated on the basis of the langrangian polynomial shape functions typically used in finite element methods.[6] The high resolution upwind discretization is constructed on the basis of the Roe approximate Riemann solver introduced in[7] generalized to the case of fluids characterized by arbitrary equations of state according to the method of Vinokur and Montagné.[8] This class of discretization schemes is particularly well suited to the computation of high Mach number flows such as those occurring in an ORC turbine. The use of unstructured grids allows for the straightforward treatment of domains of arbitrarily complex geometry. Another important feature of *zFlow* is represented by the adopted implicit time integration scheme, which allows for the computation of steady state solutions in a much more efficient way with respect to conventional explicit schemes. The gain in computational efficiency is crucial when complex equation of state are needed for an accurate flow simulation. The *zFlow* solver has been successfully validated for ideal gas simulations.[5,9] A more detailed description of the numerical methods and models implemented in *zFlow* is given elsewhere.[5]

2.2 The advanced thermodynamic models

The CFD code *zFlow* integrates a rich thermodynamic library for the calculation of properties of pure fluids and mixtures which has been extended to include the particular (secondary) thermodynamic functions required by the implicit upwind flow solver.[10] The software library[11] contains, amongst others, a cubic EoS (StanMix) and state-of-the-art multi-parameter EoS models (TPSI, RefProp). All the needed thermodynamic properties, primary and secondary, are efficiently computed from their analytical expressions.

In this study, the thermodynamic behavior of the fluid is modeled with three EoS that differ in complexity and accuracy: the polytropic ideal gas (PIG) EoS, the Peng-Robinson-Stryjek-Vera (PRSV) cubic EoS and the state-of-the-art Span-Wagner (SW) EoS. The polytropic ideal gas (PIG) law is given by:

$$P = \frac{RT}{v}, \tag{1}$$

where P is the pressure, T is the temperature and v is the specific volume. R is the specific gas constant which is defined as $R = \mathcal{R}/M$, where M is the molecular weight and $R = 8.314$ J/(molK) is the universal gas constant. The other necessary information for the calculation of all caloric properties is the ideal gas specific heat at constant pressure

$$C_P^0 = \frac{\gamma R}{\gamma - 1}. \tag{2}$$

Here, γ denotes the ratio of the specific heats, $\gamma = C_P^0/C_v^0$, where C_P^0 and C_v^0 are the dilute gas isobaric and isochoric heat capacities, respectively. The ratio γ is constant under the polytropic assumption considered here.

The Peng-Robinson-Stryjek-Vera[12] (PRSV) cubic EoS is of the form:

$$P = \frac{RT}{(v - b)} - \frac{a(T)}{v(v - b) + b(v - b)}, \tag{3}$$

where a and b are the coefficients of the contributions of, respectively, the attractive and short-range repulsive intermolecular forces. Compared to the polytropic ideal gas EoS (1), this cubic EoS allows for accurate predictions in the dense gas region (close to saturation conditions), but is not accurate close to the critical point (i.e., $P/P_c > 0.9$)

In the Stryjek-Vera modification[12] of the Peng-Robinson EoS, the temperature-dependent parameter $a(T)$ has a particular functional form that has allowed the extension of the range of applicability to the low reduced temperature region as well as to polar fluids. The main feature is that it allows for accurate estimates of vapor-pressures (within 1 % of experimental data). This reflects in an improved prediction performance of superheated vapor thermodynamic properties in the region adjacent to the saturation curve. The PRSV EoS can be used together with modern mixing rules to accurately estimate the properties of mixtures.[10,12]

For the calculation of all caloric properties, the PRSV EoS (3) is supplemented by the ideal gas contribution to the specific heat at constant pressure, which has been approximated here as a polynomial function of the temperature:

$$C_P^0(T) = A + BT + CT^2 + DT^3. \tag{4}$$

Recently, Span and Wagner[13] have developed a numerically stable multi-parameter EoS for non-polar and weakly polar fluids. This state-of-the-art EoS in the Helmholtz-explicit functional form allows for accurate computations of all relevant thermodynamic properties over the entire thermodynamic range, i.e., even close to the critical point, with the accuracy required for design and analysis of advanced technical applications. The Span-Wagner (SW) EoS has by far superior accuracy and numerical stability compared with older multi-parameter EoS's.[13] In the EoS, the reduced Helmholtz energy, i.e., $\psi = \Psi/(RT)$, is expressed as a function of the reduced density, $\delta = \rho/\rho_\mathrm{c}$, and the inverse of the reduced temperature $\tau = T_\mathrm{c}/T$. The functional form uses 12 substance specific parameters and reads:

$$\begin{aligned}
\psi(\tau,\delta) &= \psi^0(\tau,\delta) + \psi^\mathrm{r}(\tau,\delta) \\
&= \psi^0(\tau,\delta) + n_1\delta\tau^{0.250} + n_2\delta\tau^{1.125} + n_3\delta\tau^{1.500} \\
&\quad + n_4\delta^2\tau^{1.375} + n_5\delta^3\tau^{0.250} + n_6\delta^7\tau^{0.875} \\
&\quad + n_7\delta^2\tau^{0.625}\mathrm{e}^{-\delta} + n_8\delta^5\tau^{1.750}\mathrm{e}^{-\delta} + n_9\delta\tau^{3.625}\mathrm{e}^{-\delta^2} \\
&\quad + n_{10}\delta^4\tau^{3.625}\mathrm{e}^{-\delta^2} + n_{11}\delta^3\tau^{14.5}\mathrm{e}^{-\delta^3} + n_{12}\delta^4\tau^{12.0}\mathrm{e}^{-\delta^3}
\end{aligned} \tag{5}$$

Here, $n_1, \ldots, n_{12}$ are the parameters, ψ^0 represents the ideal gas contribution to the Helmholtz free energy and ψ^r accounts for the difference between real gas behavior and ideal gas behavior. Eq. (5) is valid for many classes of non-polar and weakly polar fluids and was developed by means of an optimization algorithm that considered data sets for different classes of fluids simultaneously.

Important features of (5) are:

1. The functional form (5) allows for numerically stable and consistent predictions of thermodynamic data over the entire range of interest for technical applications, therefore one and the same EoS can be used to for example design an ORC plant and for gasdynamic simulations; moreover, it has the potential to be a true reference EoS: it has been proved[14] that it can predict thermodynamic data within the uncertainty of the best available experimental data (provided that enough experimental data are available and that the optimization is done properly) and is therefore often used as a reference EoS.

2. Due to the relatively small number of substance dependent parameters, the functional form allows for fast computations of thermodynamic properties. This is an important requirement if the EoS is implemented in a thermodynamic-properties library which is used to provide data to a CFD solver, as it requires many evaluations.

3. The 12 parameters can be determined from a restricted set of experimental data; furthermore, due to its optimized functional form the equation of state can be

used to predict thermodynamic data outside the range where experimental data are available, i.e., the extrapolation behavior is good.

4. Once the Span-Wagner EoS for a substance is established, it can always be improved when additional and/or more accurate experimental data become available.

For the calculation of all caloric properties, the SW EoS (5) is supplemented by the ideal gas contribution to the specific heat at constant pressure, given by (4).

3 REAL GAS EFFECTS IN AN ORC STATOR BLADE PASSAGE

The mentioned *zFlow* program is used to investigate the influence which the three considered EoS models have on the aerodynamic performance of an ORC turbine blade. The flow field through the 2D nozzle blade of an existing ORC turbine operated with the siloxane MDM as working fluid is chosen as an example. The turbine operating conditions, which are also the prescribed boundary conditions in the simulations, are given in Table 1. The passage, as shown in Fig. 1(a), has been designed without the use of a 2D real gas CFD simulation tool and it is essentially the bottom part of a converging-diverging nozzle that has been curved in order to obtain the desired stator outflow angle.

The compressibility factor, defined as $Z = (Pv)/(RT)$, is identically equal to unity for an ideal gas; it is therefore often used to quantify the nonideality of the thermodynamic state. Only a limited portion of the expansion through this turbine stator passage occurs in the nonideal gas thermodynamic region, as indicated by the values of the compressibility factor at inlet and outlet, reported in Table 1. This might be due to the fact that a lack of real gas CFD simulation tools such as *zFlow* has limited the design of ORC turbines that operate at thermodynamic conditions that deviate further from ideality, which are potentially more thermodynamically favorable.

Table 1: Turbine operating conditions.

		Design-point	Part-load	
Expansion ratio	P_{01}/P_2, -	6	4	
Total inlet pressure	P_{01}, bar	8	8	$(P_{01}/P_c = 0.56)$
Total inlet temperature	T_{01}, °C	262.6	262.6	$(T_{01}/T_c = 0.90)$
Compressibility factor at inlet	Z_1, -	0.69	0.69	
Static outlet pressure	P_2, bar	1.333	2	
Compressibility factor at outlet	Z_2, -	0.95	0.93	

The working medium, siloxane MDM (Octamethyltrisiloxane), has a high molecular weight of $M = 236.5315$ g/mol. The PRSV EoS (3) and the isobaric specific heat relation

(4) were optimized for siloxanes to perform the thermodynamic optimization of ORCs[15] and their parameters were recently refined.[16] Parameters for SW-type EoS (5) for siloxanes were also recently optimized[16] and specific results regarding MDM will soon be reported in the open literature. For the PIG EoS model (1), a constant ratio of specific heats of $\gamma = 1.0173346$ is adopted, which is calculated from the isobaric and isochoric ideal gas specific heats evaluated at the critical temperature, as it is close to the total inlet temperature (cf. Table 1).

It should be noted that the Euler solver used in this work permits to investigate the main inviscid features of the flow field through the stator passage, which are the focus of this paper. Viscous phenomena such as boundary layers and a turbulent wake, which are present in the real flow field, can not be taken into account.

All flow solutions have converged up to at least six orders of magnitude measured in the L^2-norm of all the conserved variables.

3.1 Grid convergence study

The periodic grid is generated in a transformed domain, in which periodic boundaries are mapped into internal curves to simplify the task of obtaining periodic nodes.[17] In the transformed space the grid is generated by the front-advancing/Delaunay method[18] and then transformed back into the physical space of XY-coordinates by introducing a suitable cut, which translates into the saw-like edge of the periodic boundaries shown in Fig. 1(a). It is noted that in Fig. 1(a) the aspect ratio is distorted, because the turbine design is confidential property of the manufacturer.

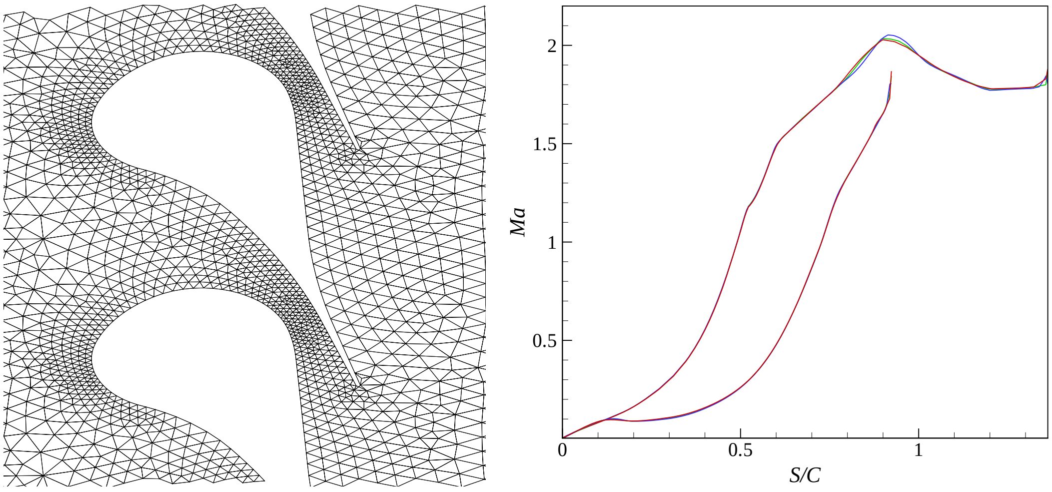

(a) (b)

Figure 1: (a) Coarse grid. The figure aspect ratio is distorted, since the turbine design is confidential property of the manufacturer. (b) Mach number distribution on the fine grid (—), the medium grid (—) and the coarse grid (—).

In order to determine the discretization error level, a grid convergence study is performed by computing the solution on three increasingly finer grids using the accurate SW EoS. The fine grid and the coarse grid are generated by, respectively, halving and doubling the number of grid elements with respect to the initial medium grid. The coarse grid consists of 1398 nodes and 2066 elements, the medium grid of 2511 nodes and 4000 elements and the fine grid of 4642 nodes and 7838 elements. Fig. 1(a) shows the coarse grid and the blade geometry. Fig. 1(b) shows the Mach number distributions solved on the coarse, medium and fine grid, for design-point operating conditions. They are plotted as a function of the reduced coordinate S/C, in which S is the curvilinear distance along the blade profile and C is the blade chord, starting from the theoretical stagnation point defined by $X/C_{ax} = 0$, where X is the axial coordinate and C_{ax} is the axial chord. From this result, it appears that the computed solution is grid-independent. The fine grid is therefore used for all subsequent simulations.

3.2 Design-point simulation

The computation on the fine grid using the accurate SW EoS is used to investigate the flow field of the expansion process at design-point operation. The two-dimensional flow field is plotted in Fig. 2 by visualizing the Mach number and superimposing the isobars and streamlines. From the inflow boundary on the left hand side of the domain, the fluid accelerates through the passage formed by the stator blade cascade to supersonic velocities. At the blade trailing edge, an over-expansion region can be observed. Further downstream, the flow is bent slightly into itself resulting in a weak oblique shock.

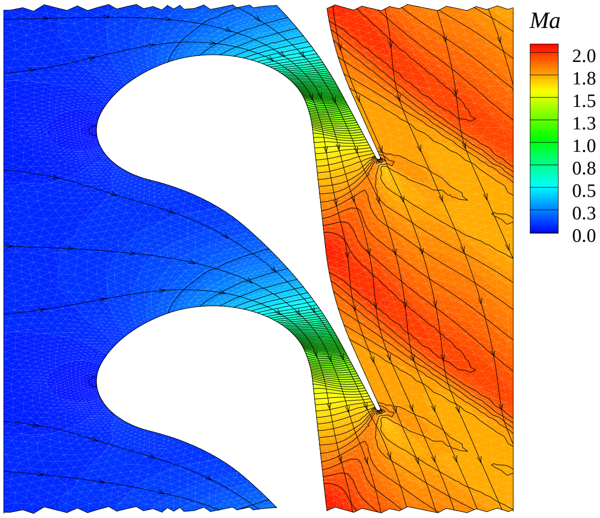

Figure 2: Flow field Mach number including isobars and streamlines at design-point operation. The figure aspect ratio is distorted, since the turbine design is confidential property of the manufacturer.

The effect of the different fluid models on the fluid dynamics is evaluated by comparing the distributions of various parameters along the blade surface. These are shown in Fig. 3 and 4.

It should be noted that this nozzle has been designed for inlet conditions corresponding to a slightly superheated vapor at a reduced pressure $P_{01}/P_c \approx 0.56$ (see Table 1), with a large expansion ratio so that the process evolves very rapidly toward lower pressure states (near ideal gas). Significant real gas effects are therefore present only in the initial phase of the expansion through the blade nozzle (i.e. only along the first half of the blade surface). The predicted performance of the nozzle blade is therefore not heavily affected by the chosen thermodynamic model even if some differences have indeed been put in evidence.

The Mach number distribution is given in Fig. 3(a). The line that indicates early expansion (with a maximum in the Mach number) pertains to the suction side of the blade, the line with retarded expansion to the pressure side. At the location $S/C = 0.52$-0.6 the Mach number distribution of the suction side does not vary smoothly, indicating irregular expansion, which might indicate an imperfection in the design of the blade.

The Mach number distribution appears surprisingly similar for all EoS models. However, in the first part of the expansion along the blade, the Mach number distribution computed with the PIG model shows a large *relative* difference with respect to the one computed with the SW EoS, as becomes apparent from Fig. 4(c). In fact, at the leading edge ($S/C = 0$), the Mach number is 10% lower according to the PIG EoS. This is caused by the fact that the first portion of the expansion process occurs in the more nonideal gas thermodynamic region, as indicated by the compressibility factor in Table 1. The initial high nonideality has, however, little effect on the absolute value of the Mach number since the latter is initially very low. Further downstream, at $S/C \approx 0.7$ on the suction side as well as at $S/C \approx 0.9$ on the pressure side, the Mach number based on the PIG EoS is 5% higher. The maximum difference in Mach number predicted by the PRSV model is only 0.5%.

The sound speed, denoted by c, is shown in Fig. 3(c). According to the PIG model, the sound speed of MDM is high ($c \approx 137$ m/s) and decreases slightly, which, under ideal gas theory, is always the case for an isentropic expansion. PRSV and SW, on the other hand, predict a much lower sound speed ($c = 93$ m/s) in the initial phase of the expansion, which is more realistic since the inlet state is close to the critical point. The initial error in the sound speed predicted by the PIG model is approximately 48%. Furthermore, as the fluid expands, PRSV and SW predict an increase in sound speed, ultimately reaching a value of $c \approx 128$ m/s. Such an increase in sound speed across an isentropic expansion can occur only for molecularly complex fluids within a certain thermodynamic region[19] as is discussed in the following.

The relative difference in Mach number among the PIG and the real gas models (SW and PRSV) is at maximum 10%, which is significant, but small compared to the relative difference in sound speed, which is at maximum 48%. This results from the fact that the higher sound speed is compensated by a velocity magnitude that is similarly higher, as is shown in Fig. 4(b). The figure shows the percentage difference of velocity magnitude for the PIG EoS with respect to the SW EoS. As the difference in sound speed decreases (Fig. 3(c)), the difference in velocity magnitude also decreases (Fig. 4(b)), thus limiting the relative difference in the Mach number (Fig. 4(c)) to a maximum of 6% further downstream. This leads to an Mach number distribution that, even in relative terms, does not differ as much between EoS models as the sound speed and the velocity magnitude.

As stated above, one of the main peculiarities of dense vapor flows of complex molecules is the variation of the speed of sound with density. The fundamental derivative, denoted by Γ, is the parameter that, if negative, indicates the possible occurrence of the so-called nonclassical gasdynamic behavior.[20,21,19] It is defined as:

$$\Gamma \equiv 1 - \frac{v}{c}\left(\frac{\partial c}{\partial v}\right)_s \tag{6}$$

Here, v is the specific volume and s is the entropy. Fluids which have $\Gamma < 0$ over a finite range of pressures and temperatures in the single-phase regime are referred to as Bethe-Zel'dovich-Thompson (BZT) fluids after the authors who first recognized the importance of (6). The molecules of these fluids have a high number of degrees of freedom, which is often the case for fluids that have a high molecular weight. Their molecular complexity enables them to exhibit nonclassical fluid dynamic behavior such as expansion shocks and compression fans.[19] For the less stringent condition $\Gamma < 1$, the isentropic relation between sound speed and temperature is inverted with respect to the ideal gas behavior: the sound speed increases across an isentropic expansion and decreases across an isentropic compression.

Fig. 3(d) shows the distribution of the fundamental derivative. The results for the SW EoS show that the entire expansion process occurs at $\Gamma < 1$, which is in accordance with the increase in sound speed observed in Fig. 3(c) for the PRSV and SW models. Initially, its value is $\Gamma = 0.56$ (SW) and $\Gamma = 0.59$ (PRSV) and it increases to $\Gamma = 0.67$. With respect to the SW model, PRSV model predicts a 5% higher Γ at the leading edge. Although MDM can be considered a molecularly complex fluid ($0 < \Gamma < 1$ in this expansion process), nonclassical fluid dynamic behavior is not possible as it is known that MDM is not a BZT fluid, i.e., $\Gamma > 0$.[10] The PIG EoS incorrectly predicts a value of 1.0087, since it is known[20] that for ideal gas (6) reduces to $\Gamma = 1/2(\gamma + 1)$.

The distribution of the pressure coefficient defined as

$$C_P = \frac{P_{01} - P}{P_{01} - P_2}, \tag{7}$$

where P_{01} is the total inlet pressure and P_2 the static outflow pressure, is shown in Fig.3(b). Its trend is similar to the one of the Mach number. Note that the same pressure values are prescribed at the inflow and outflow boundary for all EoS.

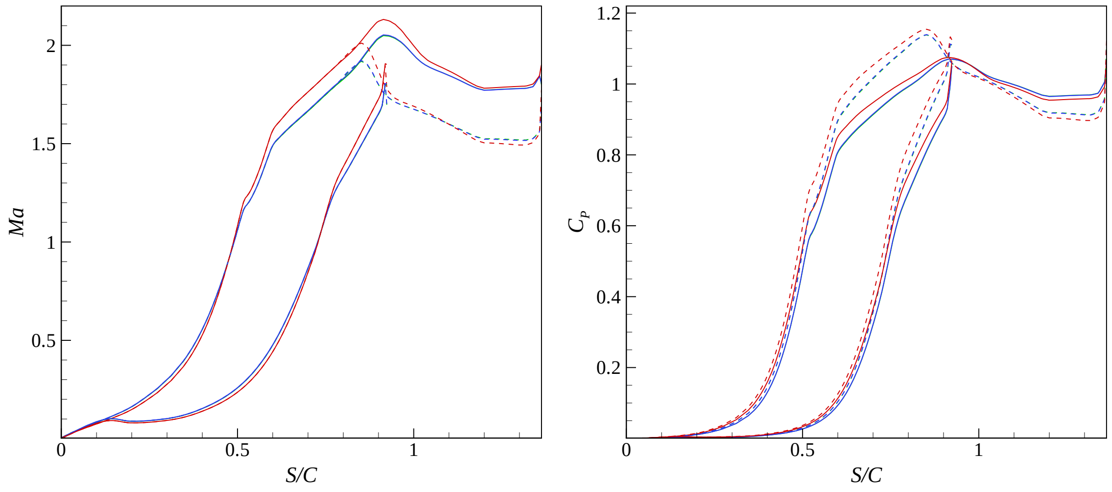

(a) Mach number (b) Pressure coefficient

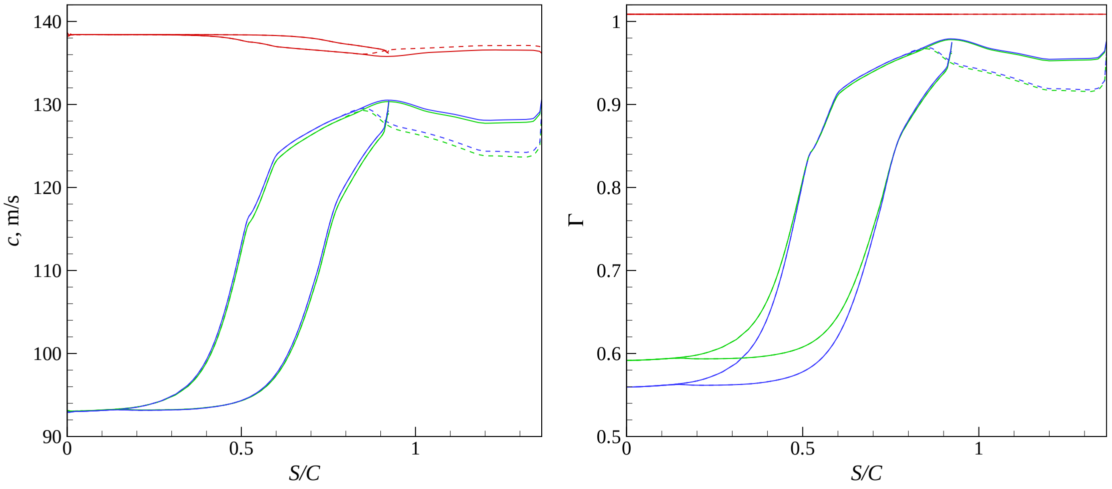

(c) Sound speed (d) Fundamental derivative

Figure 3: Blade surface distributions at design-point (continuous line) and at part-load (dashed line) based on SW (——), PRSV (——) and PIG (——).

Very large differences in densities between the EoS models can be observed in Fig. 4(d). At the leading edge, the difference based on the PIG EoS with respect to the SW EoS is as high as 30% but monotonically decreases to 3% along the rear part of the blade, as the fluid expands toward lower pressure (ideal gas) states. The large initial difference can be expected, since pressure and temperature are the prescribed variables at inflow and outflow and density depends on the EoS model. The distribution of the deviation from ideal gas in terms of density is therefore similar to the distribution of the compressibility factor shown in Fig. 4(a). The maximum difference in density predicted by the PRSV EoS with respect to the SW EoS is only 1%.

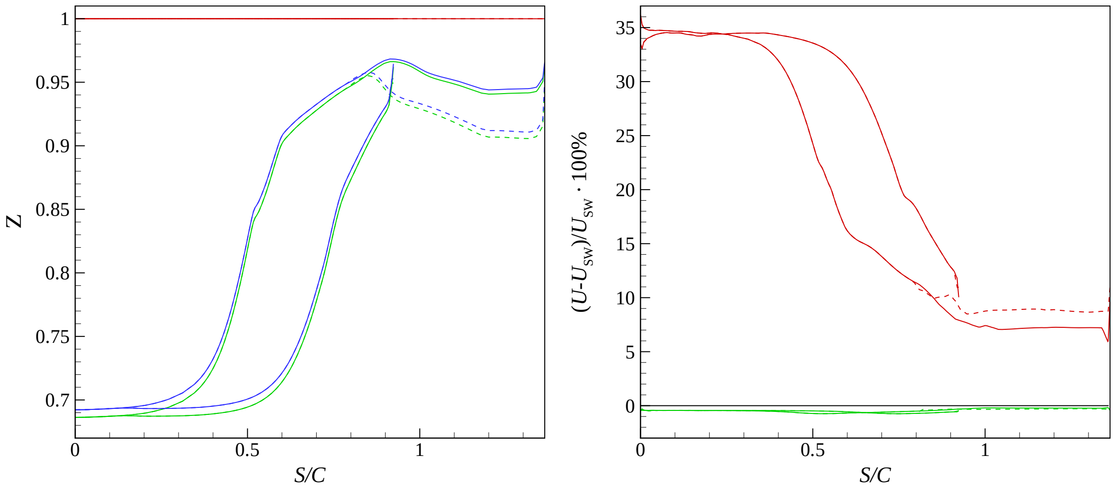

(a) Compressibility factor

(b) Velocity magnitude, relative to the SW EoS

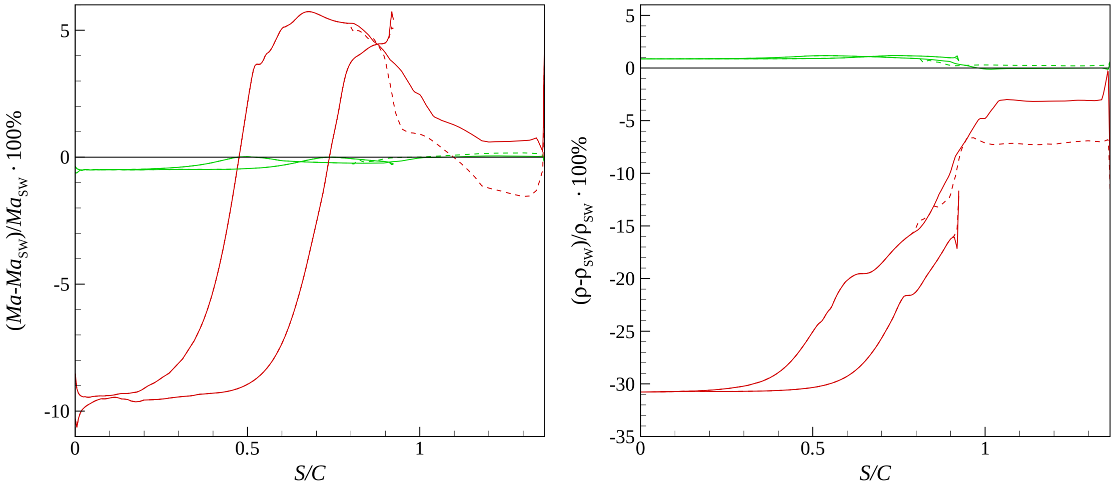

(c) Mach number, relative to the SW EoS

(d) Density, relative to the SW EoS

Figure 4: Blade surface distributions at design-point (continuous line) and at part-load (dashed line) based on SW (——), PRSV (——) and PIG (——).

The compressibility factor, denoted by Z, serves as a measure for the deviation from ideal gas behavior. Its distribution in Fig. 4(a) puts into evidence that only the first part (approximately $S/C < 0.5$) of the expansion process is very nonideal ($0.65 < Z < 0.8$). Consequently, in this initial part the fluid dynamic parameters (Mach, velocity, density) computed based on the PIG EoS have the largest deviation with respect to the SW EoS. As the fluid rapidly expands toward lower pressure states the nonideality is reduced to only $Z = 0.94$ (near ideal gas).

The absolute magnitude of the velocity, based on the accurate SW EoS, increases from almost zero at the leading edge ($S/C = 0$) to 253 m/s at $S/C = 1$. The relative difference in the magnitude of the velocity between the EoS models, shown in Fig. 4(b), is initially as high as 35% for the PIG model. This difference slowly decreases to 7% at the rear part of the blade and is 8% at the outflow boundary. Nonetheless, this error in the predicted outflow velocity magnitude can lead to an incorrect design of the rotor blades, resulting in reduced turbine efficiency. For the PRSV EoS, this error is less than one percent.

The outflow angle, denoted by β, is defined as the angle between the flow direction at the outflow boundary and the axial direction. The outflow angle along the reduced Y-coordinate (scaled with the pitch value), given in Fig. 5(a), shows an oscillatory behavior due to the weak oblique shock waves in the flow field (see Fig. 2). Computations based on the PIG model result in an average outflow angle error of 1.5°, which may lead to a less-than-optimal design of the rotor blades. For PRSV, the error in the outflow angle negligible.

The Mach number along the outflow boundary is plotted in Fig. 5(b). It shows that the PIG EoS predicts, on average, a 2% higher Mach number which may result in a slightly stronger shock wave. This is investigated for part-load operation in Section 3.3. The deviation of the outflow Mach number based on the PRSV EoS with respect to the SW EoS is negligible.

Table 2 also lists the percentage deviations of the mass flows with respect to the values computed based on the SW EoS. The mass flow relative to the one based on the SW EoS is 6.8% lower for the PIG EoS and 0.4% higher for the PRSV EoS. If this ORC stator blade were designed using the PIG model, the large error in the predicted relation of mass flow with respect to pressure ratio would also affect the operation of the other components in the ORC cycle, possibly leading to suboptimal cycle performance.

Table 2: Percentage difference of the mass flow ($\text{DEV}_{\dot{m}}$) and pressure loss coefficient ($\text{DEV}_{C_{PL}}$) for the PRSV and PIG EoS models with respect to the values computed based on the SW EoS. The pressure loss coefficient is defined as the mass-weighted average over the outflow boundary of $C_{PL} = 1 - P_{02}/P_{01}$, where P_{01} is the total inlet pressure and P_{02} the local total outflow pressure.

	Design-point	Part-load	
EoS model	$\text{DEV}_{\dot{m}}$, %	$\text{DEV}_{\dot{m}}$, %	$\text{DEV}_{C_{PL}}$, %
PRSV	0.43	0.43	-1.15
PIG	-6.76	-6.76	5.67

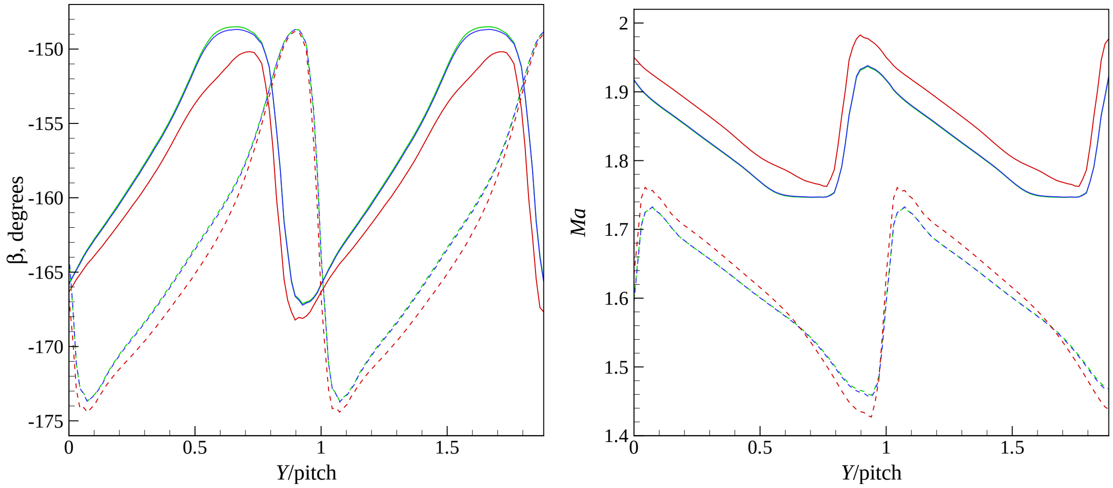

(a) (b)

Figure 5: Outflow angle (a) and Mach number (b) along the transverse coordinate (reduced by the pitch) at design-point (continuous line) and at part-load (dashed line) based on SW (—), PRSV (—) and PIG (—).

3.3 Part-load simulation

It is assumed that for part-load operation, the total pressure at the inlet is controlled to remain at $P_{01} = 8$ bar. In this particular part-load condition, the pressure ratio, P_2/P_{01}, is reduced from 6 to 4, so that the backpressure is higher (see Table 1).

The computation on the fine grid using the accurate SW EoS is again used to investigate the flow field of the expansion process, in this case for part-load operation. The two-dimensional flow field is plotted in Fig. 6 by visualizing the Mach number and superimposing the isobars (using same pressure interval as used in Fig. 2) and streamlines. It can be observed that, with respect to design-point operation, lower Mach numbers are obtained for part-load, but that, judging from the isobars, the (reflected) shock wave is stronger.

The effect of the different fluid models on the fluid dynamics at part-load is again evaluated by comparing the distributions of various relevant parameters along the blade surface, shown in Figs. 3 and 4. Here, dashed lines pertain to part-load distributions. It can be observed that in all blade distributions the initial part ($S/C < 0.75$) is the same for design-point and part-load, because the stator nozzle is choked. An exception is the pressure coefficient (Fig. 3(b)), since its definition, given by (7), depends on the outlet pressure P_2. The difference with respect to design-point operation is that since the pressure ratio is reduced, firstly, the Mach number after expansion is lower (Fig. 3(a)) and, secondly, the outflow pressure is higher so that the final part of the expansion occurs in the nonideal thermodynamic region for a larger portion (see Fig. 4(a)). This leads

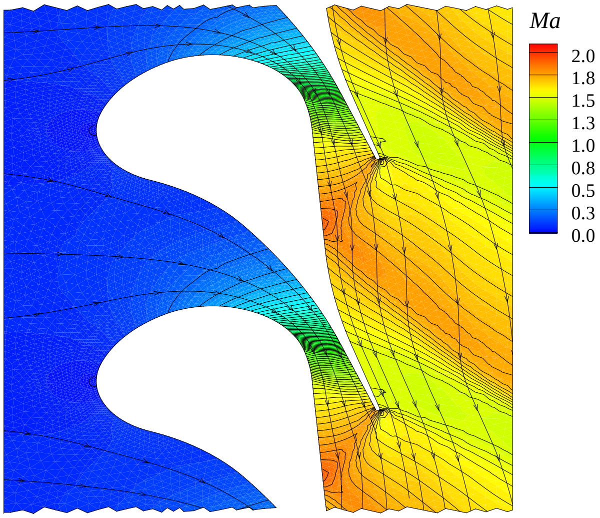

Figure 6: Flow field Mach number including isobars and streamlines at part-load operation. The figure aspect ratio is distorted, since the turbine design is confidential property of the manufacturer.

to a larger deviation of sound speed, fundamental derivative, velocity magnitude and density if the PIG model is compared to the SW and PRSV models. For the relative difference in Mach number (Fig. 3(a)), this deviation is not uniformly higher, but rather differently distributed. At the blade trailing edge and at the outflow boundary (Fig. 5(b)) the difference in Mach number between the PIG and SW EoS is smaller (even in relative terms) than for design-point operation. A similar phenomenon can be observed for the outflow angle in Fig. 5(a). This is surprising, since, for part-load, the final part of the expansion is more nonideal than for design-point, so that a larger deviation would be expected.

The larger and steeper variation (i.e. less uniform) in Mach number (Fig. 5(b)) and flow angle (Fig. 5(a)) along the outflow boundary for the PIG EoS shows that the simulation based on the PIG EoS exhibits stronger shock waves, as was noted earlier. This is confirmed by the total pressure loss coefficient (Table 2), which is 6% higher for the PIG EoS. The deviation of the outflow Mach number based on the PRSV model with respect to SW model is negligible. The total pressure loss coefficient based on PRSV (Table 2) is only 1% lower than the one of the SW model.

The choked conditions for both design-point and part-load can also be concluded from the equal mass flows as stated in Table 2. Consequently, the same differences in mass flow are observed between all the EoS models as happens for the design-point case.

4 CONCLUSIONS

The novel *zFlow* program is used to investigate the influence of the polytropic ideal gas (PIG) equation of state (EoS), the Peng-Robinson-Stryjek-Vera (PRSV) cubic EoS and the state-of-the-art Span-Wagner (SW) EoS on the predicted aerodynamic performance parameters and flow features of an existing ORC turbine blade that operates, at least partly, in a thermodynamic region where the ideal gas assumption does not hold.

The fluid dynamic results are very similar for the SW and PRSV EoS. The PIG EoS, on the other hand, shows large relative differences in almost all parameters, when compared to the accurate SW EoS. As expected, the PIG EoS underpredicts the density in the initial portion of the expansion process by more than 30%.

The Mach number distribution along the blade surface appears surprisingly similar for all mentioned EoS models. This is due to the fact that, although the first portion of the expansion process occurs in the more nonideal gas thermodynamic region, the Mach number here is low, so that the initial high nonideality has little effect on the absolute value of the Mach number. Moreover, the flow is chocked and so the Mach number is equal to unity at the nozzle throat. Since the distance from the leading edge (where M = 0) to the throat is small, more or less the same profiles are observed. The final portion of the expansion process occurs at lower pressure states that are much closer to the ideal gas region, thus limiting the effect on the, at this point, high absolute Mach number. The effect of the initial high nonideality does become apparent in the initial portion of the distribution of the *relative* difference in the Mach number among the PIG and the real gas models (SW and PRSV), where it is as high as 10%. Nonetheless, this is small compared to the relative difference in sound speed, which is at maximum 48%. This results from the fact that the incorrectly higher sound speed predicted by the PIG EoS is compensated by a velocity magnitude that is similarly higher. As the process evolves toward lower pressure (close to ideal gas) states and the relative difference in sound speed among the PIG and the real gas models decreases, the relative difference in velocity magnitude also decreases, thus limiting the relative difference in the Mach number.

Very large differences in densities among the PIG and the real gas models (SW and PRSV) can be observed in the initial portion of the expansion. The large initial difference can be expected, since pressure and temperature are the prescribed variables at inflow and outflow and density depends on the EoS model. For the latter reason, the distribution of the pressure coefficient shows only small differences among EoS models and its trend is similar to the one of the Mach number.

In part-load conditions, the PIG EoS predicts stronger shock waves, shown by a 6% higher total pressure loss coefficient and the less uniform distributions of Mach number and flow angle along the outflow boundary.

The application of the PIG model results in an average stator outflow angle deviation of 1.5° with respect to the real-gasa models, which may lead to a less-than-optimal design of the rotor blades. The predicted mass flow is 6.8% lower for the PIG EoS and 0.4% higher for the PRSV EoS, both compared to the one predicted by the accurate SW EoS. If this ORC stator blade were designed using the PIG EoS, the large error in the predicted relation of mass flow with respect to pressure ratio would also affect the operation of the other components in the ORC cycle, possibly leading to suboptimal cycle performance.

For the simulation and design of this type of ORC expansion process, which operates partly in the nonideal gas thermodynamic region characterized by a compressibility factor of $0.69 < Z < 0.95$, the use of the PRSV EoS appears well suited, since the fluid dynamic results are very similar for the SW and PRSV EoS. The use of the PIG EoS, on the other hand, leads to appreciable errors in the predicted aerodynamic performance parameters and flow features. For potentially more efficient supercritical ORC cycles, the use of the PRSV in the simulation of the turbine flow might also lead to relevant inaccuracies, since in this case a larger portion of the expansion process occurs in a highly nonideal thermodynamic region.

Viscous simulations of similar turbines are planned, for which the *zFlow* program will be extended to the numerical solution of the Reynolds-averaged Navier-Stokes equations.

References

[1] J. Hoffren, T. Talonpoika, J. Larjola, and T. Siikonen. Numerical Simulation of Real-Gas Flow in a Supersonic Turbine Nozzle Ring. *J. Eng. Gas Turbine Power*, 124:395–403, 2002.

[2] M. Cirri, P. Adami, and F. Martelli. Development of a CFD Real Gas Flow Solver for Hybrid Grid. *Int. J. Numer. Methods Fluids*, 47(8-9):931–938, March 2005.

[3] A. Arnone M. Cecconi P. Boncinelli, F. Rubechini and C. Cortese. Real Gas Effects in Turbomachinery Flows - A Computational Fluid Dynamics Model for Fast Computations. In *Transactions of the ASME*, volume 126, pages 268–276, 2004.

[4] C. Cravero and A Satta. A CFD Model for Real Gas Flows. In *ASME Turbo Expo, Munich, Germany*, pages 1–10, New York, May 2000. ASME, ASME.

[5] P. Colonna and S. Rebay. Numerical simulation of dense gas flows on unstructured grids with an implicit high resolution upwind Euler solver. *Int. J. Numer. Meth. Fluids*, 46(7):735–765, 2004.

[6] V. Selmin. The node-centred finite volume approach: bridge between finite differences and finite elements. *Comp. Meths. Appl. Mech. Eng.*, 102:107–138, 1993.

[7] P. L. Roe. Approximate Riemann solvers, parameter vectors, and difference schemes. *J. Comput. Phys.*, 43:357–372, 1981.

[8] M. Vinokur and J. L. Montagné. Generalized flux-vector splitting and Roe average for an equilibrium real gas. *J. Comput. Phys.*, 89:276, 1990.

[9] P. Colonna, A. Guardone, J. Harinck, and S. Rebay. Numerical Investigation of Dense Gas Effects in Turbine Cascades. In *Proceedings of the 15th U.S. National Congress on Theoretical and Applied Mechanics*, 2006. (in press).

[10] P. Colonna and P. Silva. Dense Gas Thermodynamic Properties of Single and Multi-Component Fluids for Fluid Dynamics Simulations. *J. Fluids Engrg.*, 125(3):414–427, May 2003.

[11] P. Colonna and T. P. van der Stelt. FluidProp: A program for the estimation of thermophysical properties of fluids. Energy Technology Section, Delft University of Technology, The Netherlands (`www.fluidprop.com`), 2005.

[12] R. Stryjek and J. H. Vera. PRSV: An Improved Peng-Robinson Equation Of State For Pure Compounds And Mixtures. *Can. J. Chem. Eng.*, 64:323–333, 1986.

[13] R. Span and W. Wagner. Equations of State for Technical Applications. I. Simultaneously Optimized Functional Forms for Nonpolar and Polar Fluids. *Int. J. Thermophys.*, 24(1):1–39, January 2003.

[14] R. Span and W. Wagner. Equations of State for Technical Applications. II. Results for Nonpolar Fluids. *Int. J. Thermophys.*, 24(1):41–109, January 2003.

[15] G. Angelino and P. Colonna. Multicomponent Working fluids for Organic Rankine Cycles (ORCs). *Energy*, 23(6):449–463, 1998.

[16] P. Colonna, N. R. Nannan, A. Guardone, and E. W. Lemmon. Multi-parameter Equations of State for Selected Siloxanes. *Fluid Phase Equilib.*, 2006. (in press).

[17] A Guardone and S Rebay. Unstructured periodic grid generation. In *Proceedings of the ECCOMAS CFD 2006 Conference, Egmond aan Zee, The Netherlands*, 2006. (in press).

[18] S. Rebay. Efficient Unstructured Mesh Generation by Means of Delaunay Triangulation and Bowyer–Watson Algorithm. *J. Comput. Phys.*, 106(1):125–138, 1993.

[19] P. Colonna and A. Guardone. Molecular Interpretation of Nonclassical Gasdynamics Phenomena in the Vapor Phase under the van der Waals Polytropic Model. *Phys. Fluids*, 2006. (in press).

[20] J. F. Monaco, M. S. Cramer, and L. T. Watson. Supersonic Flows of Dense Gases in Cascade Configurations. *J. Fluid Mech.*, 330:31–59, 1997.

[21] B. P. Brown and B. M. Argrow. Application of Bethe-Zel'dovic-Thompson Fluids in Organic Rankine Cycle Engines. *J. Propul. Power.*, 16(6):1118–1123, November-December 2000.